Journal of *Marine Science and Engineering*

MDPI

Article

Integrated Seismic–Electromagnetic Data Fusion and Inversion for the Characterization of Gas Hydrate Reservoirs in the Shenhu Sea Area, South China Sea

Miaomiao Meng [1,2], Wei Deng [1,2], Kaijun Xu [3], Zhongliang Wu [1,2,*], Jin Liang [1,2,*] and Jianping Li [1,2]

1 National Engineering Research Center of Gas Hydrate Exploration and Development, Guangzhou Marine Geological Survey, Ministry of Natural Resources, Guangzhou 511458, China; 18811309981@126.com (M.M.); hahens@163.com (W.D.); lijianping14@126.com (J.L.)
2 Guangzhou Marine Geological Survey, China Geological Survey, Guangzhou 510075, China
3 School of Geosciences, China University of Petroleum, Qingdao 266580, China; xkj79@upc.edu.cn
* Correspondence: WZLLZW1997@163.com (Z.W.); liangjin1999@163.com (J.L.)

Abstract

The integrated fusion and inversion of seismic data and marine controlled-source electromagnetic (MCSEM) data can identify the gas hydrate distributions. However, due to differences in observation systems and scales between seismic and MCSEM data, current fusion methods have failed to effectively address the critical issue of physical property variation within gas hydrate reservoirs. This research seeks to consolidate the two datasets into a cohesive observational framework. By transforming the MCSEM data into low-frequency constraints applicable to seismic impedance inversion, it is possible to realize an effective integrative interpretation that combines both seismic and MCSEM data. Using a 3 km-long seismic dataset and MCSEM data from the Shenhu Sea area in the South China Sea as a case study, we apply the Poisson blending algorithm to integrate seismic and MCSEM data, enabling precise identification and characterization of gas hydrate reservoirs and underlying gas-bearing fluids. The gas hydrate saturation results, derived from seismic inversion constrained by MCSEM data, demonstrate strong consistency with well logging and geological interpretation. This concordance validates the efficacy of the integrated fusion and inversion methodology and highlights its advantages in accurately predicting the spatial distribution of gas hydrate enrichment. The developmental positions of deep gas-bearing fluid pathways, coupled with the fault locations within the free gas zone and gas hydrate-bearing layer, play significant roles in the heterogeneous enrichment of gas hydrates. This research provides important technical and theoretical support for the precise and efficient prediction of gas hydrate reservoirs.

Keywords: gas hydrate reservoir; gas hydrate accumulation; marine controlled-source electromagnetic; seismic inversion; Shenhu area

Academic Editor: Yanghui Li

Received: 26 June 2026
Revised: 20 August 2026
Accepted: 31 August 2026
Published: 4 September 2026

1. Introduction

Natural gas hydrate is a new type of clean energy with abundant reserves and high energy density. It also holds significant research importance in the prevention of geological disasters and global climate change [1–4]. Currently, several countries are conducting gas hydrate trial production projects, aiming to industrialize gas hydrate production. One of the key issues that urgently needs to be addressed is how to accurately locate large-scale, high-quality gas hydrate deposits. At present, the most widely used data for exploring and studying gas hydrate deposits are seismic data. By identifying Bottom Simulating Reflectors (BSRs) on seismic profiles, the distribution of gas hydrates can be generally inferred. However, seismic data often cannot precisely determine the variation in reservoir physical properties within them. With the rapid development of geophysical exploration technologies, multi-coverage seismic data (such as travel-time inversion, full waveform inversion, and AVO techniques) have been widely applied, clarifying velocity indicators for gas hydrate layers. Nevertheless, the absence of low-frequency information in seismic data often leads to multiple possible interpretations.

In recent years, the development of marine controlled-source electromagnetic (MCSEM) technology has made it possible to accurately identify gas hydrate deposits in marine areas. MCSEM, a branch of marine electromagnetic methods, offers advantages such as high resolution in shallow layers and strong capability to detect high-resistivity anomalies [5–8]. It can image the electrical structure of gas hydrate stability zones, which have higher resistivity compared to surrounding sediments, allowing for more accurate identification and characterization of gas hydrate. Additionally, MCSEM can relatively accurately determine gas hydrate saturation, because MCSEM data directly measures the absolute value of resistivity, rather than the relative wave impedance difference as in seismic data. Therefore, MCSEM has been widely recognized within the industry as an effective complementary method to seismic exploration of gas hydrates [8–13]. While seismic data offer high resolution, they cannot precisely delineate the degree of gas hydrate enrichment within the deposits. In contrast, MCSEM can better characterize variations in gas hydrate saturation within gas hydrate deposits. The combined interpretation of seismic data and MCSEM data can leverage their respective advantages, reduce the multiple solutions of a single geophysical method, and enhance the reliability of the interpretation [14,15]. By combining different types of geophysical data for interpretation, it becomes possible to thoroughly integrate the various geophysical features of the target, greatly enhancing the identification precision.

The development of data fusion processing technology has provided new approaches for the integration of geophysical data and the establishment of more accurate geophysical model bodies [16,17]. Previous studies on the fusion of different geophysical data have significantly improved the efficiency and accuracy of geological interpretation, such as gravity and magnetic data [18,19], combinations of seismic, resistivity, and neutron capture data [20], integrated analysis of seismic and transient electromagnetic data, as well as combined gravity and seismic analysis [21,22]. Previous studies on seismic-MCSEM data integration for gas hydrate characterization have predominantly relied on overlay display methods for visual comparison [14,15]. These approaches superimpose seismic profiles and resistivity sections but achieve only visual co-rendering rather than mathematical fusion. We propose a Poisson blending-based fusion workflow that performs gradient-domain mathematical fusion rather than simple overlay. In addition, we construct a physically constrained low-frequency model from MCSEM data to guide seismic inversion, thereby bridging the resolution gap between the two datasets.

The Shenhu Sea area is China's leading gas hydrate research zone and has already completed two production tests (Figure 1A) [23]. For the first time, we have collected MCSEM and seismic data in the Shenhu Sea area, which provide a solid data foundation to accurately characterize the gas hydrate reservoir. Therefore, this study uses the Shenhu production test area as a case study, aiming to achieve high-precision characterization of gas hydrate reservoirs by integrating seismic and MCSEM data. This study also explores the accumulation model of gas hydrate reservoirs and validates the effectiveness of integrating seismic and MCSEM data.

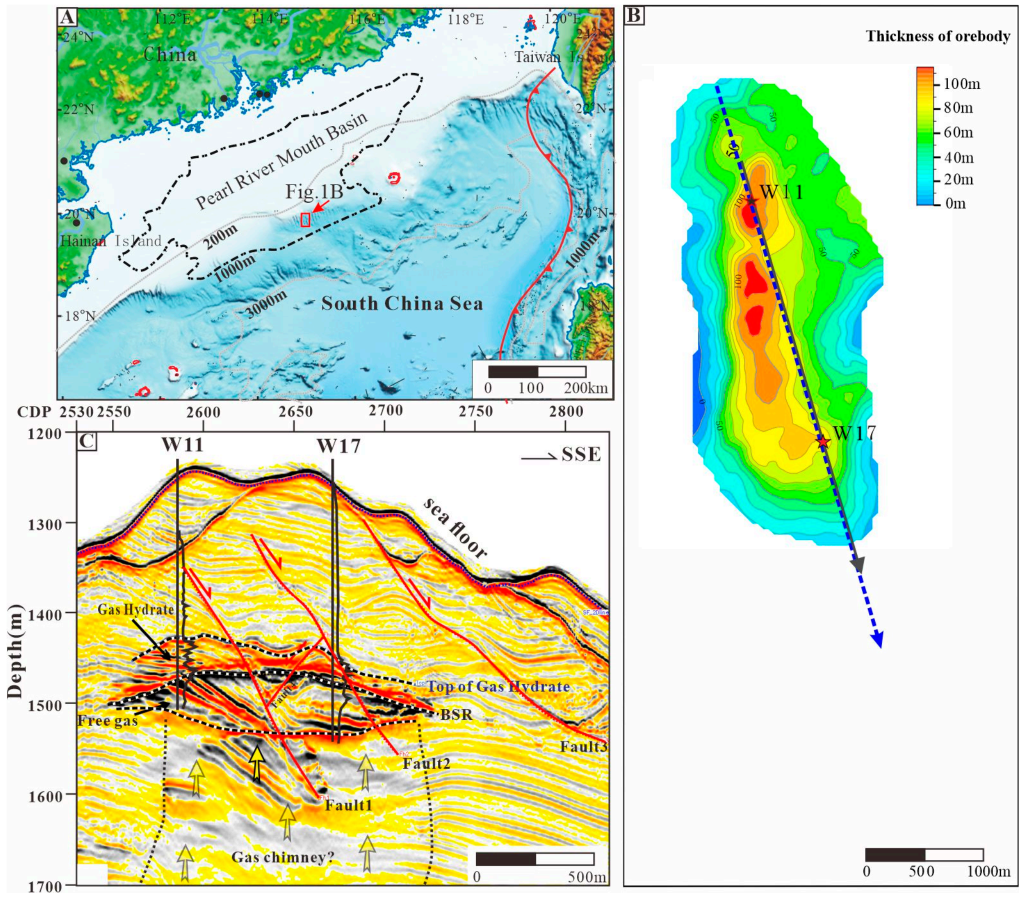

Figure 1. (**A**) The location of the gas hydrate production test area in the Shenhu area of the South China Sea; (**B**) the thickness distribution of the W11-17 gas hydrate orebody (cited after reference [23]); Note: the black arrow line shows the location of the seismic profile in (**C**), and Figure 2, and the dashed blue arrow line shows the location of the MCSEM profile in Figure 3A; (**C**) the characterization of the W11-17 gas hydrate orebody based on seismic interpretation. Note: The yellow arrow shows the direction of gas-containing fluid flow; the red half arrow shows fault.

2. Geological Setting

The Shenhu gas hydrate enrichment area is located on the northern continental slope of the South China Sea, structurally within the Baiyun Sag of the Pearl River Mouth Basin (Figure 1A). The water depth ranges from 1000 to 1500 m, with a relatively steep terrain and an average slope of up to 3% [24]. It is characterized by a group of canyon channels distributed in a nearly NW-SE direction. The seabed temperature ranges from 3.3 to 3.7 °C, with a geothermal gradient of 45 to 67 °C/km. The water pressure at the seabed exceeds 10 MPa. These conditions meet the favorable temperature and pressure conditions for gas hydrate accumulation [25,26].

During the Cenozoic era, the Pearl River Mouth Basin experienced multiple regional tectonic events, including the Shenhu Movement, Zhuqiong Movement, South China Sea Movement, and Dongsha Movement. These events resulted in the Cenozoic tectonic evolution of the Baiyun Sag exhibiting distinct characteristics of early fault subsidence followed by later flexural subsidence [27]. In the Shenhu Sea area, sedimentary layers developed sequentially from bottom to top, including terrestrial facies, marine-terrestrial transitional facies, and marine facies, showing an overall transgressive trend [28–30]. The Baiyun Sag is rich in gas sources. The Paleogene Eocene Wenchang Formation and Lower Oligocene Enping Formation contain mature to highly mature source rocks; meanwhile, Neogene sediments such as the Zhujiang Formation and Hanjiang Formation have relatively lower organic matter maturity and can serve as biogenic gas source rocks. Both deep thermogenic gas and shallow biogenic gas provide ample gas sources for hydrate formation in the study area [31,32]. Neotectonic movements induced plastic flow of thick, overpressured mud shale in the Paleogene, forming large-scale BSR activity zones that led to the development of mud diapirs and gas chimneys. The arching activity of the BSR caused the formation of arch-shaped anticlines at various depths, generating high-angle faults and vertical fracture systems. These structures provide migration and transport pathways conducive to gas hydrate formation [33].

The coastal shallow sea, semi-deep sea, and deep sea clastic rock deposits are composed of the Pliocene Wanshan Formation and the Quaternary Qionghai Formation. The Quaternary period mainly developed fine-grained turbidite deposits, which serve as the primary reservoir layers for gas hydrate. The BSR, indicative of gas hydrate presence, is widely distributed along the base interface of the Quaternary [34]. The test mining body primarily develops diffusely distributed gas hydrate within the natural levee muddy silt reservoirs located on canyon ridges, forming a deposit area of approximately 6.8 km^2, buried at depths of 201–278 m below the seafloor, with a maximum thickness of about 77 m and an average saturation of 45.2% [23,35].

3. Data and Methods

3.1. Data

This study utilizes two-dimensional seismic data and MCSEM data from the Shenhu gas hydrate production test area in the South China Sea (Figure 1C).

The time-domain 2D seismic data spans a total length of 3675m (Figure 2A), with CDP numbers ranging from 2530 to 2824, totaling 295 traces at a trace interval of 12.5 m. The vertical sampling interval is 2 ms and contains 3001 samples. The vertical depth after the time-to-depth conversion is approximately 2337 m. The frequency ranges from 5 to 150 Hz, with a dominant frequency of 50 Hz. The maximum amplitude is 1.66113, the minimum amplitude is −2.1736, and the root-mean-square (RMS) amplitude is 9.98984 × 10^{-2}. The RMS velocity data are consistent with the 2D seismic data, with a maximum velocity of 1843.73 m/s, a minimum of 1386.4 m/s, and an average velocity of 1552.3 m/s.

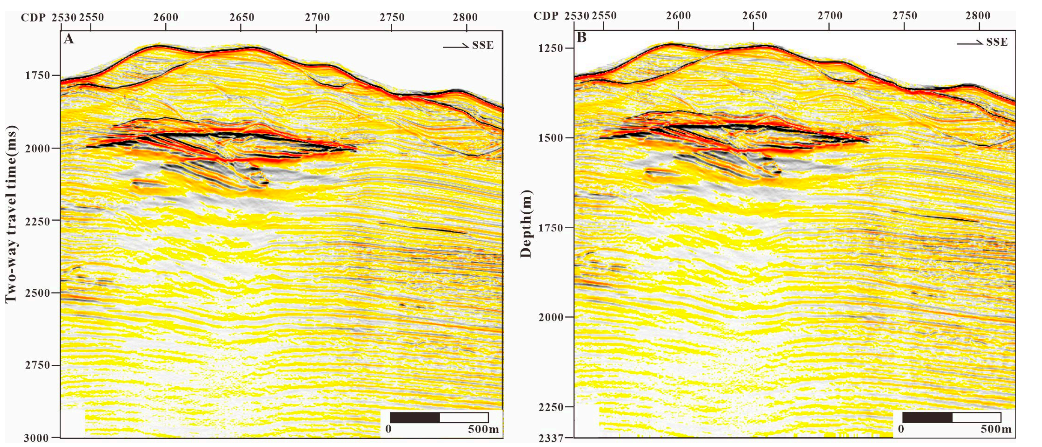

Figure 2. Seismic data in the Shenhu Sea area. (**A**) Two-dimensional seismic profile in time domain; (**B**) two-dimensional seismic profile in depth domain. Note: See the location of the seismic profile in Figure 1B.

The MCSEM data were independently collected by the Guangzhou Marine Geological Survey. The effective profile length is 3 km, with measurement points spaced every 300–500 m; the vertical depth range is 0 to 3000 m (Figure 3). There are 8 acquisition points at an excitation frequency of 8 Hz, with numerical depth intervals of 50 m. At an excitation frequency of 1.5 Hz, the numerical intervals are also 50 m. The reliable depth of the 1.5 Hz two-dimensional inversion profile is approximately 3 km, while that of the 8 Hz two-dimensional inversion profile is approximately 2 km [36].

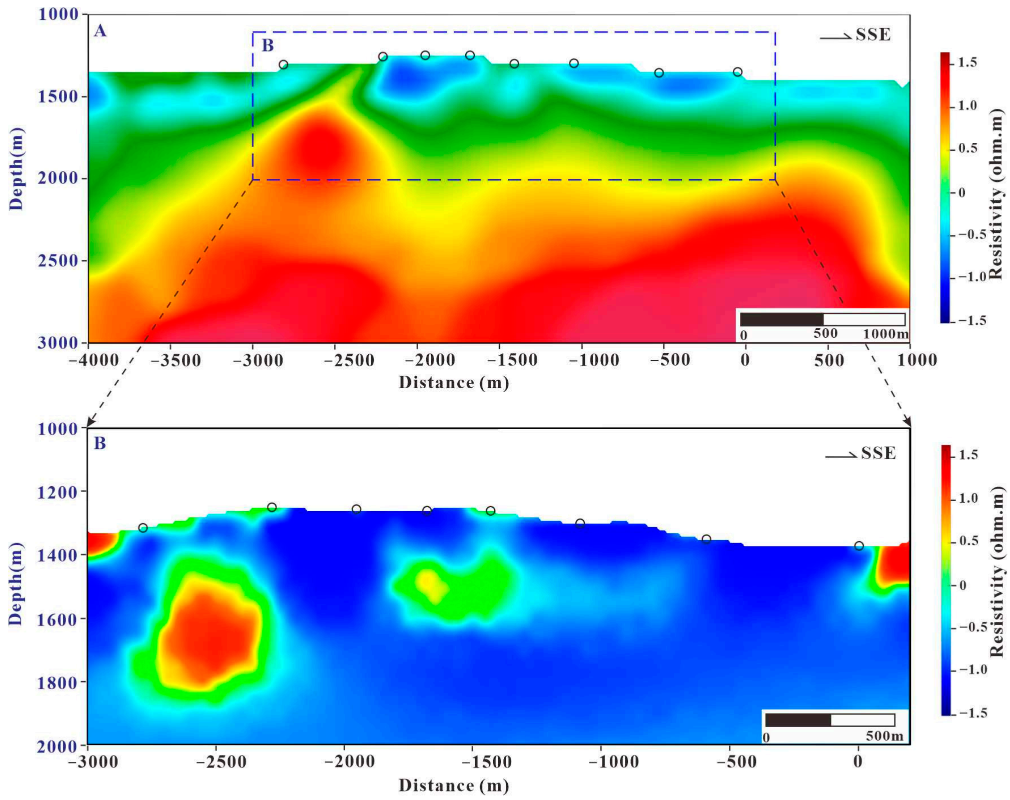

Figure 3. (**A**) The inversion resistivity distributions of 1.5 Hz MCSEM data resulting from data densification processing; (**B**) the inversion resistivity distributions of 8Hz MCSEM data resulting after data densification processing. Note: The circles represent the locations of the acquisition points.

3.2. Methods

To ensure format consistency, it is necessary to perform format conversion on both seismic and MCSEM data. This involves converting seismic data from the time domain to the depth domain, as well as transforming MCSEM resistivity data into SEGY format to align with the seismic data. Then, by applying the Poisson fusion algorithm, seismic and MCSEM data are fused, enabling accurate gas hydrate identification and interpretation.

3.2.1. Conversion of Seismic Data

Depth conversion is the process of transforming seismic data from the time domain to the depth domain. This process involves multiple steps, including seismic data processing and velocity analysis, with continuous optimization of the conversion [37]. The velocity data in the time domain treats the strata thickness corresponding to each sampling time interval in the profile as a thin layer. Using the RMS velocity Formula (1), the layer velocity Formula (2) for each thin layer can be derived. Depth conversion is then performed from top to bottom, where the thicknesses of each thin layer are cumulatively added to obtain the interface depth using Formula (3), ultimately achieving the conversion of seismic data from the time domain to the depth domain (Figure 2B).

$$v_{R,n} = \sqrt{\frac{\sum_{i=1}^{n} \Delta t_i v_i^2}{\sum_{i=1}^{n} \Delta t_i}} \quad (1)$$

$$v_n = \frac{t_{0,n} v_{R,n}^2 - t_{0,n-1} v_{R,n-1}^2}{t_{0,n} - t_{0,n-1}} \tag{2}$$

$$h_n = \sum_{i=1}^{n} \left(\frac{1}{2} \Delta t \times v_i \right) \tag{3}$$

where $v_{R,n}$ is the root-mean-square velocity at the i-th sampling point (m/s), v_n is the layer velocity, t_i is the two-way travel time at the i-th sampling point (s), Δt_i is the time interval between sampling points, and h_n is the cumulative depth.

3.2.2. MCSEM Data Processing and Conversion

In order to facilitate the integration of MCSEM resistivity data with seismic data, it is necessary to correlate the resistivity data with the seismic data sets. To achieve this, the resistivity data must be resampled so that the sampling intervals match those of the seismic data. After conducting an in-depth analysis of the seismic SEGY data format, we rewrote the MCSEM resistivity data to create resistivity files based on the SEGY data format.

3.2.3. The Integrated Fusion of Seismic Data and MCSEM Data

The purpose of integrating seismic and MCSEM data is to fully leverage the advantages of both seismic and electromagnetic data in identifying gas hydrate reservoirs, while preserving the high-fidelity information from each. With the advancement of image fusion technology, numerous fusion methods have emerged, including the alpha blending algorithm, wavelet transform, intensity–hue–saturation (IHS) transform, and Poisson fusion algorithm [38,39]. Compared to traditional algorithms such as wavelet fusion and IHS transform, Poisson fusion offers several advantages [16]: it preserves texture information through gradient transfer and exhibits stronger noise resistance, as it is insensitive to local noise, which makes it particularly well-suited for processing geophysical data with interference.

In this study, seismic amplitude data in the depth domain serves as the source image, providing high-resolution structural gradient information, while the inverted MCSEM resistivity profile serves as the target image, offering absolute resistivity values that reflect the true electrical properties of the subsurface. Prior to fusion, both datasets are normalized to a common range of [0, 1] using min–max normalization to eliminate numerical bias caused by differences in physical units and magnitude scales between seismic amplitudes and resistivity values.

The fusion region, which acts as the mask for the Poisson blending operation, is defined as the full overlapping area between the seismic depth profile and the MCSEM resistivity profile. A binary mask M(x,z) is generated such that M = 1 within the fusion region and M = 0 outside. Dirichlet boundary conditions are applied along the boundary of the fusion region, where pixel values are constrained to equal the target image values, ensuring a seamless transition at the fusion boundaries.

Within the fusion region, the gradient field is computed from the seismic source image using central finite differences. The Poisson equation is discretized with a five-point finite-difference stencil and solved using the Gauss–Seidel iterative method combined with successive over-relaxation. Iterations terminate when the maximum relative change between successive iterations falls below 10^{-4}. The resulting fused image simultaneously captures the structural gradients from seismic data and the absolute resistivity values from MCSEM data.

The formula for the Poisson fusion algorithm is as follows:

$$\min \iint_{\Omega} \|\nabla f - \nabla u\|^2 \tag{4}$$

Here, $\bigtriangledown f$ represents the gradient of the composite image, and $\bigtriangledown u$ is the gradient of the target image to be inlaid. The above equation indicates that within each region of the overlapping area Ω, they should be as equal as possible, meaning the difference should be minimized. Additionally, the pixel values of the composite image and the composite background are equal along the boundary of the overlapping area.

To find the solution to the above equation, that is, to find the extremum of Formula (5), proceed as follows: substitute into the Euler–Lagrange equation and take partial derivatives with respect to x and y to obtain the following expressions:

$$F = \|\nabla f - \nabla u\|^2 = (f_x - u_x)^2 + \left(f_y - u_y\right)^2 \quad (5)$$

$$\frac{\partial F}{\partial x} = 2(f_x - u_x)(f_{xx} - u_{xx}) = 0 \quad (6)$$

$$\frac{\partial F}{\partial \mathrm{y}} = 2\left(f_y - u_y\right)\left(f_{yy} - u_{yy}\right) = 0 \quad (7)$$

If the sums of f_x and u_x, and f_y and u_y are unequal, then the sum of $(f_{xx} - u_{xx})$ and $(f_{yy} - u_{yy})$ is zero. By adding the partial derivatives, the new expression can be obtained as:

$$f_{xx} + f_{yy} = u_{xx} + u_{yy} \quad (8)$$

Therefore, the following solution, which satisfies the boundary constraint conditions, is expressed as:

$$\Delta f = div(\nabla u) = u_{xx} + u_{yy} \quad (9)$$

Here, Δ represents the Laplacian operator, $\Delta f = f_{xx} + f_{yy}$ denotes the Laplacian of f, and div represents the divergence of u.

3.2.4. Seismic Inversion Constrained by MCSEM Data

In the early stages of gas hydrate exploration, there is often a lack of well logging, core samples, and other data. Seismic inversion without well constraints can help delineate favorable gas hydrate zones during the initial exploration phase. The most critical steps in seismic inversion include seismic wavelet extraction, low-frequency model construction, and parameter testing. Among these, the construction of the low-frequency model is the most crucial. However, seismic data generally lack low-frequency information. Typically, a high-precision tomographic velocity model or a full waveform inversion velocity model with a broader frequency band is used for this purpose, but significant uncertainties still remain. Given the advantage of MCSEM data in capturing low-frequency background information, the resistivity profiles obtained from MCSEM data can be converted into velocity profiles using the relationship among resistivity, gas hydrate saturation, and acoustic impedance. This velocity profile can then serve as a low-frequency constraint for seismic inversion to obtain elastic parameters such as acoustic impedance and velocity. The inversion results obtained in this way reflect not only the characterization of the background field by MCSEM data but also retain the superior vertical resolution of seismic data. Based on the inversion of acoustic impedance and velocity, gas hydrate reservoirs can be finely characterized, and the spatial distribution of gas hydrate saturation can be obtained.

To verify the fusion effectiveness of the seismic and MCSEM data, we first perform seismic inversion relying solely on the constraint of MCSEM data. The inversion results are then compared with well-logging data. The low-frequency model is obtained based on MCSEM data: the Archie equation is used to transform the MCSEM resistivity profile into a saturation profile, which is then converted into an acoustic impedance profile using the saturation–acoustic impedance relationship. This impedance–saturation relationship is based on actual logging data from the Shenhu study area and is considered highly reliable. The formula is:

$$S_{gh} = 8.477e^{-5} \times I_p - 0.91 \quad (10)$$

Here, I_p represents P-impedance.

This paper employs the constrained sparse spike inversion method to obtain wave impedance. The key steps include well-logging calibration, wavelet extraction, low-frequency model construction, and inversion. Well-logging calibration is conducted on the seabed and the top/bottom interface of gas hydrate. Since the seismic data have undergone zero-phase processing, the wavelets selected for this purpose share the same dominant frequency (50 Hz) as the seismic data (Ricker wavelets). The construction of the low-frequency model differs from conventional methods. Typically, the low-frequency model is derived from well-logging data; however, in this study, a wave impedance low-frequency model obtained through MCSEM data transformation is used as the low-frequency constraint for inversion. During the inversion process, to compensate for the missing low-frequency components of the seismic data, an 8 Hz low-frequency model is incorporated. The regularization parameter of the wavelet is set to 1, and a hard-constraint inversion method is adopted, with the error range controlled within 10%. Multiple key indicators, such as residuals, are used to evaluate the inversion process. After each inversion, it is necessary to verify whether significant valid information remains in the residual profile and to simultaneously assess the lateral and vertical continuity of the inversion results.

4. Results

4.1. Process of Seismic and MCSEM Data

4.1.1. Conversion of Seismic Data from Time Domain to Depth Domain

The two-dimensional seismic profile in the time domain is basically zero for the shallow part (less than 1600 ms), representing the area above the seabed (Figure 2A). Based on the RMS velocity data, the seismic data in the time domain were converted to the depth domain through time–depth conversion to obtain the seismic profile in the depth domain (Figure 2B). The calculated maximum depth of the seismic data is 2337 m.

4.1.2. Comparison of MCSEM Data at Different Frequencies

In electromagnetic exploration, frequency affects the detection depth and spatial resolution. Low-frequency signals can detect deeper targets but with reduced resolution, while high-frequency signals have shallower detection depth but significantly improved resolution. Comparing the overall resistivity distribution characteristics from the inversion results of the acquired 1.5 Hz and 8 Hz electromagnetic survey lines shows good consistency, but there are obvious differences in some local areas (Figure 3A). The inversion results of the 8 Hz electromagnetic survey line exhibit gradual changes in resistivity, which better align with the variations in geological electrical structures (Figure 3B). In contrast, the 1.5 Hz inversion results show more abrupt changes in resistivity, especially in shallow areas, where high-resistivity anomalies appear as strip-like distributions, which clearly do not conform to the geological electrical structure variations.

Since low-frequency detection penetrates deeper and high-frequency detection offers higher resolution in shallow parts, we combine the advantages of both frequencies: for depths shallower than 2 km, the resistivity from the 8 Hz MCSEM inversion data is primarily used for detailed characterization of gas hydrate deposits; for depths greater than 2 km, the resistivity from 1.5 Hz MCSEM inversion data is mainly used for in-depth study of deep fluid distribution and accumulation patterns of gas hydrate deposits.

4.1.3. MCSEM Data Processing and Conversion

The resistivity profile is derived from MCSEM data, with a lateral length of 5 km and a vertical depth of 3 km. The corresponding data file contains 101 points laterally with a spacing of 50 m, and 61 points vertically with a depth interval of 50 m. By applying data densification processing to the electromagnetic data, two densified resistivity profiles are obtained (Figure 3A,B). Then, the densified resistivity data are converted into SEGY data format, corresponding to CDP traces numbered 2464 to 2864, totaling 401 traces. Compared with the seismic profile, the MCSEM data extend 66 traces (825 m) beyond the left side and 40 traces (500 m) beyond the right side. To load the MCSEM data into seismic interpretation software Geoframe2012, we extended the 295-trace two-dimensional seismic line outward, extending 66 traces to the northwest and 40 traces to the southeast, corresponding to CDP traces numbered 2464 to 2864, totaling 401 traces.

4.2. Comprehensive Interpretation of Seismic and MCSEM Data

By matching the seismic data with MCSEM data, extracting features through cross-correlation analysis, and performing Poisson fusion calculations, the seismic–MCSEM data are deeply integrated (Figure 4).

4.2.1. Geological Characteristics of the Gas Hydrate Deposit

The upper and lower boundaries of the gas hydrate deposit, the underlying free gas zone, the gas chimney, and four faults are delineated using two-dimensional seismic data (Figure 1C). The bottom interface of the gas hydrate-bearing layer (known as BSR) displays medium to strong amplitude and medium to high continuity in seismic reflections. These reflections are approximately parallel to the seabed and exhibit a characteristic oblique intersection with the stratigraphic layers, consistent with typical BSR features. The gas hydrate deposit situated above the BSR is characterized by medium to weak amplitude and medium to low continuity on the seismic profile (Figure 1C). Below the BSR, the region exhibiting medium to strong amplitude or blank reflections corresponds to the distribution of the free gas zone. Additionally, the gas chimney is identified by weak-amplitude, low-frequency reflections with a downward pull-down effect beneath the free gas zone. While seismic data effectively outline the general distribution patterns of gas hydrate deposits, they are limited in resolving spatial variations in saturation within the gas hydrate-bearing layer, differences in enrichment levels, and the intensity and spatial distribution of gas fluids in the underlying strata.

Figure 4B shows the interpreted results after integrating the seismic profile (Figure 1C) with the resistivity profile from 8 Hz MCSEM data. Gas hydrate has higher resistivity compared to the surrounding sediments, so the resistivity from MCSEM data can accurately delineate the existence of gas hydrate. The fusion of seismic and resistivity data reveals that the high-frequency inversion results of resistivity anomalies correspond well with seismic reflection anomalies. It can be seen that the resistivity within the gas hydrate-bearing zone is not uniformly distributed; there are three relatively high-resistivity anomaly zones (the white circles in Figure 4B): a prominent high-resistivity anomaly on the left side, and two smaller high-resistivity anomaly zones in the middle of the gas hydrate reservoir. This uneven distribution of high-resistivity anomalies indicates variations in saturation within the gas hydrate reservoir.

4.2.2. Distribution Characteristics of Gas-Bearing Fluids

The gas-bearing fluid pathways also exhibit higher resistivity compared to the surrounding rock, making resistivity a more accurate indicator for characterizing gas-bearing fluid pathways. As seen in the fusion image (Figure 4B), the high-resistivity anomaly regions located below the gas hydrate stability zone are interpreted as the migration pathways of gas sources for the formation of overlying gas hydrate. Within the gas hydrate deposit, there is also a pronounced high-resistivity anomaly beneath the main high-resistivity zone, clearly indicating gas-bearing fluid pathways. Notably, the high-resistivity anomaly on the left side inside the gas hydrate deposit is relatively stronger, suggesting that the gas-bearing fluid flux from below has a significant impact on gas hydrate saturation (Figure 4B). Additionally, it can be observed that the range of gas chimneys identified in the seismic profile does not completely correspond to the fluid pathway range identified in the fusion profile (Figures 1C and 4B). This indicates that the boundary of the gas chimney interpreted from seismic data does not necessarily represent the actual gas-bearing fluid pathways, highlighting the advantage of fusion in identifying fluid pathways. The deep high-resistivity anomalies reflect the electrical structure of the basement, faults, and gas-bearing fluid pathways (Figure 4A). The multiple migration pathways of gas lead to variations in gas hydrate saturation distribution within the hydrate deposits in the Shenhu Sea area.

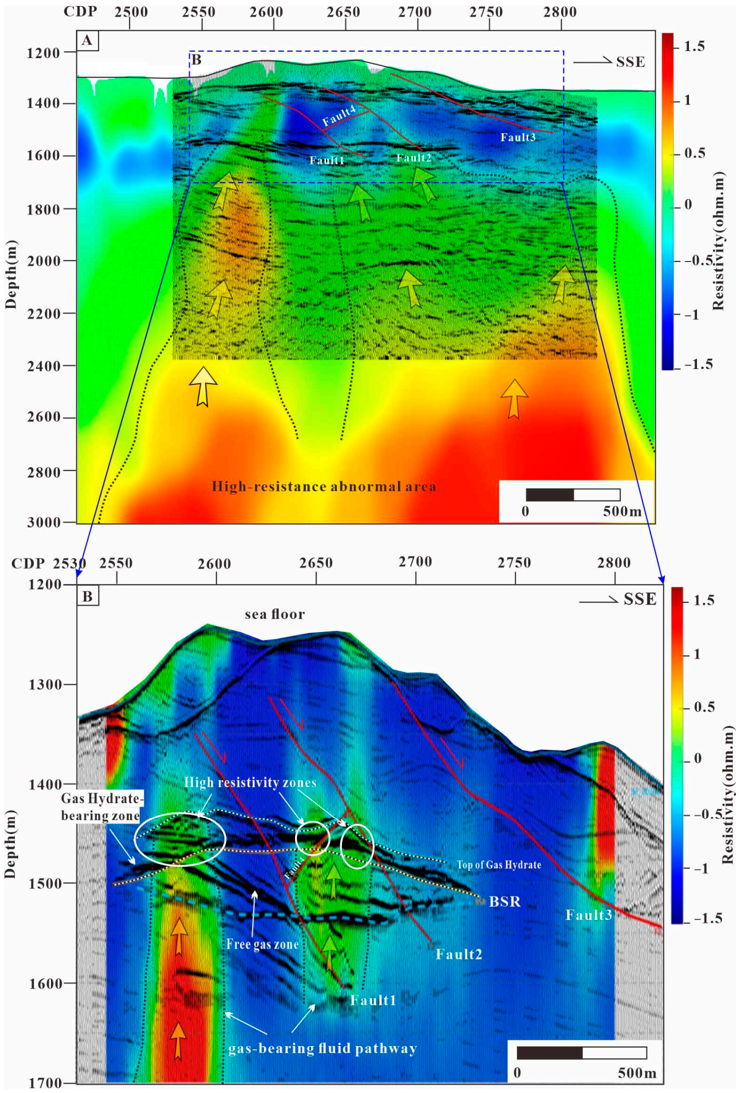

Figure 4. Fusion effect diagrams of seismic data and MCSEM data. (**A**) Fusion effect diagram of seismic data and inversion 1.5 Hz MCSEM data, and the comprehensive geological interpretation; see location in Figure 1B. (**B**) Fusion effect diagram of seismic data and inversion 8 Hz MCSEM data and two-dimensional seismic profiles, and the comprehensive geological interpretation. Note: The yellow arrow shows the direction of gas-containing fluid flow; the white circles show the high-resistivity anomaly zones within the gas hydrate-bearing zone.

5. Discussion

5.1. Prediction Accuracy of Fusion and Inversion of Seismic and MCSEM Data

By utilizing the BSR seismic reflection characteristics, the bottom interface of the gas hydrate can be identified, and the top interface of the gas hydrate reservoir can be inferred based on the positive polarity reflections above the BSR. However, it is impossible to know the physical property parameters of the gas hydrate and the heterogeneity within the reservoir. Additionally, the velocity is overly sensitive to free gas, which is unfavorable for analyzing the migration pathways of gas-bearing fluids. Since the gas hydrate-bearing layer has higher resistivity compared to the surrounding sediments, resistivity measurements more accurately characterize the depth of the top boundary and the lateral extent of high-resistivity bodies. By integrating seismic and resistivity responses of gas hydrate deposits, the presence of gas hydrate can be confirmed. Subsequently, leveraging the higher resistivity characteristic of gas hydrate, combined MCSEM data can offer a more comprehensive description of the spatial distribution and accumulation features of gas hydrate, significantly enhancing the reliability of interpretation (Figure 4).

To evaluate the impact of inversion parameter selection on the final results, we conducted a sensitivity analysis of these parameters. The low-frequency model plays a crucial role in the inversion process. In this study, we used a low-frequency model derived from MCSEM data and integrated it with seismic frequency band information (Figure 5). The seismic frequency band ranges from 5 to 150 Hz, with the highest frequency currently incorporated into the low-frequency model being 8 Hz. If the frequency of the low-frequency model is reduced to 3 Hz, the inversion result corresponds to the light-green curve in Figure 5A; if the frequency is increased to 10 Hz, the inversion result corresponds to the dark-green curve in Figure 5A. The red curve in the figure represents the impedance measured at well W11. The low-frequency model significantly influences the results. To better constrain the inversion outcomes, we applied a hard constraint, ensuring that the inversion results remain within ±20% of the regional background values, thereby reducing the non-uniqueness of the inversion. The resulting curves, shown as the green curves in Figure 5B, align more closely with the measured logging data.

To verify the advantages of integrated seismic–MCSEM data analysis over using seismic data alone, we first conducted a round of acoustic impedance inversion using only seismic data (Figure 6A). Due to the lack of low-frequency information in seismic data, the inversion results can only reveal the relative relationships between local stratigraphic interfaces, making it impossible to accurately reflect properties such as gas hydrate thickness and saturation. Specifically, prior logging and coring analyses have basically mapped out the spatial distribution of the gas hydrate reservoir: the gas hydrate thickness at well W11 is large (about 90 m), while smaller at well W17 (about 55 m) [40]. However, conventional seismic inversion results present two issues: (1) High-impedance zones A1 and A2 represent gas hydrate-bearing layers interpreted from seismic data, but the conventional seismic inversion shows that the gas hydrate-bearing layer in zone A1 is thinner than zone A2, which is clearly opposite to the gas hydrate thickness confirmed by drilling (Figure 6A). (2) Zone A3 is interpreted seismically as a gas layer below the BSR, but seismic inversion often shows a high impedance anomaly there (Figure 6B). Drilling confirms that the high impedance anomaly below the gas hydrate-bearing layer is merely caused by local reflections in the seismic data, not a gas hydrate response.

Since seismic data reflect the relative relationships above and below local stratigraphic interfaces rather than absolute impedance differences, purely seismic inversion struggles to characterize gas hydrate reservoirs in detail accurately. Comparing the results of integrated seismic–MCSEM inversion with those from seismic-only inversion clearly demonstrates the advantages of the integrated approach (Figure 6): (1) At zones A1 and A2, the integrated inversion effectively distinguishes between thick and thin gas hydrates and provides a detailed characterization of the wave impedance within the thick gas hydrate layer at well W11. The wave impedance at zone A2 is lower, indicating a lower gas hydrate saturation, which aligns more closely with actual well log data. (2) Compared to the seismic-only inversion results, the impedance anomalies at zone A3 are significantly reduced. In fact, the overall high-value anomalies below the BSR are noticeably diminished, which better matches the actual geological conditions. At zone A3, there is a gas layer whose resistivity is lower than that of the gas hydrate layer, and its impedance is also lower than that of the gas hydrate layer. Therefore, high impedance anomalies below the BSR should theoretically be less frequent, and the integrated inversion results correspond better with geological understanding.

The consistency between the integrated inversion results and geological understanding is influenced by both MCSEM and seismic data. Previous studies have shown that thick gas hydrate layers exhibit significant resistivity anomalies, while thin gas hydrate layers show weaker resistivity anomalies [25,41]. Therefore, incorporating this background into seismic inversion can effectively compensate for the lack of background trend constraints. Stratigraphic information mainly comes from seismic data, and the inversion results not only reflect the advantage of seismic data in vertical resolution but also accurately characterize the internal structure of the gas hydrate-bearing layer, which cannot be achieved by MCSEM data alone. Thus, the inversion results effectively integrated the strengths of MCSEM data in obtaining absolute formation values and background trends and the advantage of seismic data in detailing the fine internal structure of the gas hydrate-bearing layer. This provides practical technical support before drilling for exploring new areas, improving drilling success rates, and reducing non-uniqueness.

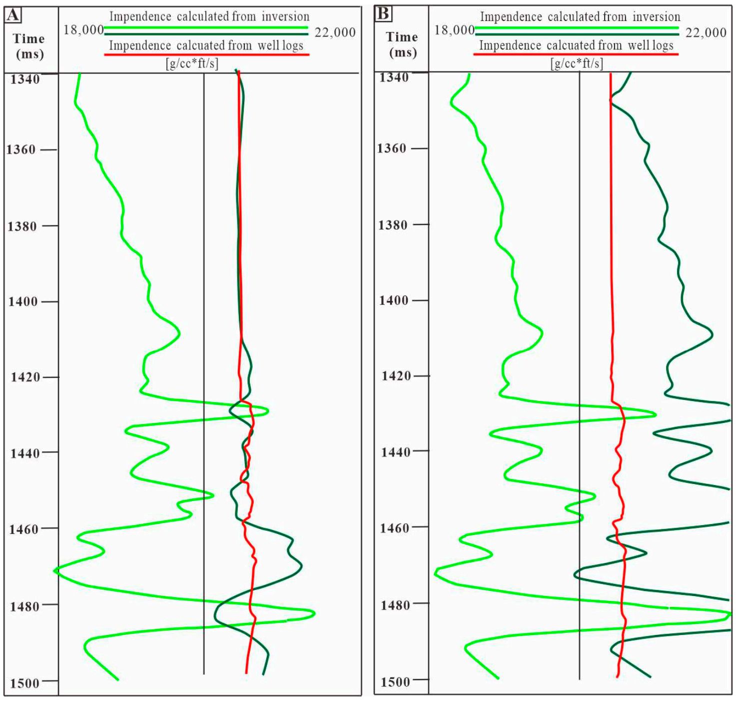

Figure 5. Sensitivity analysis of the low-frequency model: (**A**) measured impedance curve from Well W11 (red curve), inversion impedance curve at 3 Hz (light-green curve), and inversion impedance curve at 10 Hz (dark-green curve); (**B**) inversion results under hard constraints. Note: The black line shows the location of well W11 in seismic data (crossline 2586, inline 1453).

Furthermore, the gas hydrate saturation at location W11 was calculated using the wave impedance obtained from seismic–MCSEM fusion inversion (Figure 6C). Overall, the saturation closely matches the well log saturations. This result indicates that the seismic–MCSEM fusion technology can achieve true saturation inversion, enabling detailed regional evaluation of gas hydrate. Therefore, the mature application of this technology is expected to significantly reduce exploration costs and improve operational efficiency.

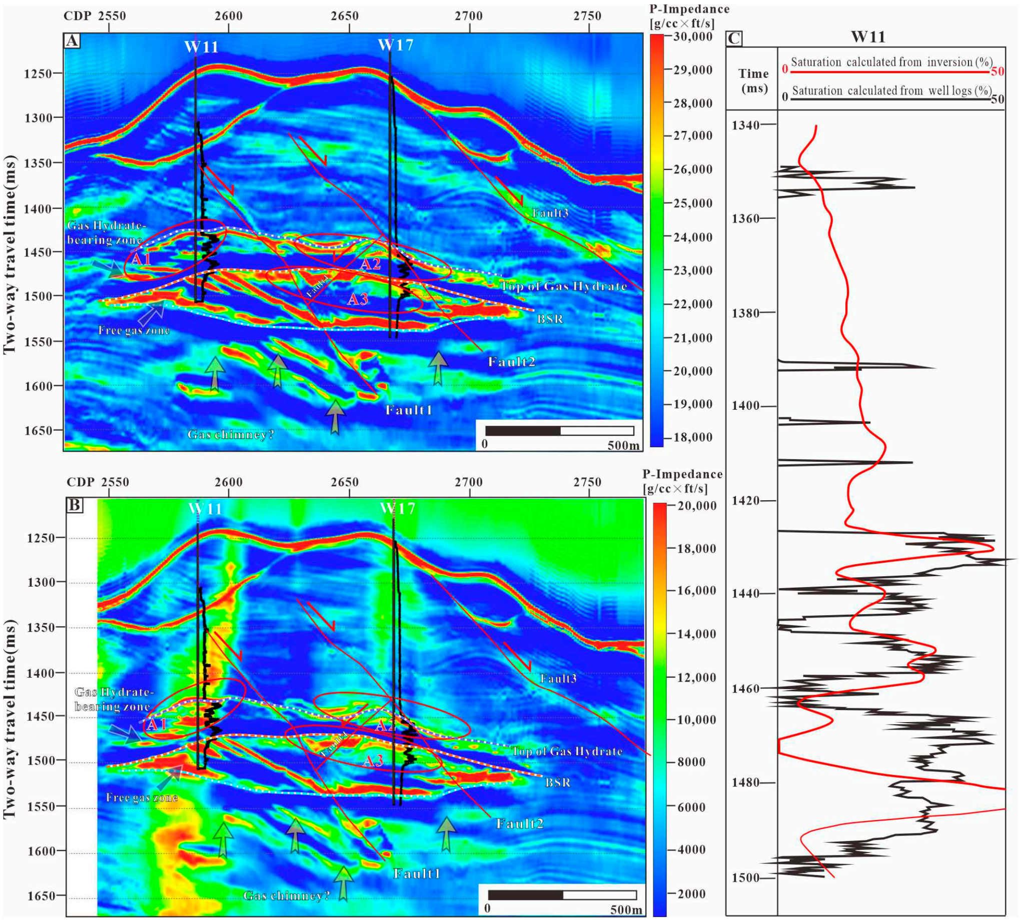

Figure 6. (**A**) Seismic-only inversion results. (**B**) Seismic–MCSEM fusion inversion results. (**C**) Comparison of gas hydrate saturation from seismic–MCSEM fusion inversion and well-logging interpretation. Note: The black curves in the inversion profiles represent the variations in resistivity for W11 and W17.

5.2. The Formation Mechanism of Gas Hydrates Heterogeneous Enrichment

Most scholars believe that the enrichment and accumulation of high-saturation gas hydrate deposits in the Shenhu area are controlled by abundant thermogenic gas sources and efficient fluid migration and transport systems [41,42]. When deep gas sources are sufficient, an efficient fluid migration pathway plays a crucial role in the enrichment and accumulation of gas hydrate. Some researchers argue that, compared to widely distributed gas chimneys, faults have a greater impact on gas hydrate distribution [43]; others suggest that faults control the distribution of gas chimneys, which in turn jointly control the high-saturation enrichment of gas hydrate reservoirs [44–46]. However, there has been relatively little research on the variation in gas hydrate saturation enrichment within a single gas hydrate orebody. The integrated seismic–MCSEM data fusion and inversion in this study provide improved characterization of the internal variations within gas hydrate reservoirs and the distribution patterns of underlying fluids.

Previous research indicates that the gas hydrate orebody is characterized by being thicker in the northwest and thinner in the southeast [23], with gas hydrate saturation showing the greatest thickness around well W11 in the northwest, followed by well W17, and there is a noticeably lower saturation zone between wells W11 and W17 (Figure 1B,C). The integrated seismic–MCSEM data and logging data reveal a distinct high-resistivity anomaly distributed vertically in the deep section near well W11.

Based on the seismic profile, the seismic–MCSEM fusion image, and the outcomes of the wave impedance inversion conducted solely with seismic data (Figures 1C, 4B and 6A), it is not feasible to accurately determine the gas distribution within the free gas zone and the primary conduits of gas-bearing fluids beneath it. Fortunately, the differential distribution patterns of the free gas zone and the underlying gas-bearing fluids can be discerned from the seismic–MCSEM fusion image and the fusion inversion image (Figures 4A and 6B): the free gas zone beneath the gas hydrate-bearing layer exhibits high-resistivity anomalies at both W11 and W17, with the anomaly being particularly prominent at W11. Consequently, we postulate that the influx of deep gas-bearing fluids is greater at W11 than at W17, and upon entering the free gas zone, these fluids become dispersed under the influence of Faults 1, 2, and 4 at W17, thereby hindering their accumulation and the formation of gas hydrates with high saturation levels at W17. In summary, the developmental positions of deep gas-bearing fluid pathways, coupled with the fault locations within the free gas zone and gas hydrate-bearing layer, play significant roles in the heterogeneous enrichment of gas hydrates.

5.3. The Strengths and Limitations

Seismic exploration remains one of the most important and effective methods for gas hydrate investigation. However, long-term practice has shown that relying solely on seismic data for predicting physical parameters still faces many challenges. This study utilizes the integrated processing of MCSEM and seismic data for gas hydrate identification and prediction, demonstrating the significant role of seismic–MCSEM fusion technology in detailed gas hydrate surveys. Nevertheless, from a practical perspective, the following limitations still exist:

The MCSEM provides resistivity data but with low resolution, while seismic data offer high resolution but lack low-frequency information. How to unify data at different scales and enhance the effectiveness of their integration remains a critical challenge that needs to be addressed in the future.

In this study, the Archie formula and the fitted impedance–saturation relationship are used to calculate the final results, which inevitably introduces uncertainty. The primary sources of error are the constants in the Archie formula and the assumption that the fitted relationship accurately represents the entire study area. Since the gas hydrate reservoir type in the Shenhu Sea area is pore-filling and the lithology is relatively homogeneous, saturation results calculated from well data can be applied to the same reservoir. However, if significant spatial heterogeneity exists in the actual hydrate distribution, alternative approaches must be adopted to mitigate these errors.

Information obtained from two-dimensional seismic and MCSEM profiles is limited. Integrating and inverting three-dimensional data would offer a more comprehensive spatial characterization of gas hydrate distribution. Transitioning from 2D to 3D introduces specific challenges related to increased complexity and computational demands. Nevertheless, the fundamental methodology developed in this 2D study can be directly extended to 3D applications.

Further validation of the role of seismic–electromagnetic data fusion technology in long-term gas hydrate monitoring is needed. Compared to well logging, integrated seismic–MCSEM interpretation is expected to become a cost-effective and feasible solution. Leveraging the respective advantages of seismic and electromagnetic data, monitoring at different times can achieve accurate descriptions of changes in gas hydrate physical parameters, thereby providing technical support for real-time development decision-making.

6. Conclusions

Seismic data and marine controlled-source electromagnetic (MCSEM) data can reveal the distribution characteristics of gas hydrate from different perspectives. Combining the two can effectively reduce the limitations of using a single geophysical method, thereby significantly improving the accuracy and reliability of interpretation. The conclusions of this study are as follows:

(1) The fusion of seismic and MCSEM data through the Poisson fusion algorithm enhances the accuracy and reliability of interpreting the heterogeneous enrichment within gas hydrate reservoirs and the distribution characteristics of underlying gas-bearing fluids.
(2) The gas hydrate saturation results obtained from seismic inversion constrained by MCSEM data align well with well logging and geological understanding, confirming the effectiveness of the integrated inversion of seismic and MCSEM data and its advantages in predicting gas hydrate-enriched distributions.
(3) Through the fusion and inversion of seismic and MCSEM data, it has been clarified that the positions of deep gas-bearing fluid pathways, together with the fault locations within the free gas zone and gas hydrate-bearing layer, play significant roles in the heterogeneous enrichment of gas hydrates.

With advancements in MCSEM equipment development, the integrated fusion of seismic and MCSEM methods will play an increasingly important role in the exploration and production of gas hydrates in the future.

Author Contributions: Conceptualization, Z.W. and W.D.; methodology, K.X.; software, K.X.; validation, M.M., W.D. and K.X.; formal analysis, W.D. and K.X.; investigation, J.L. (Jin Liang); resources, J.L. (Jianping Li); data curation, J.L. (Jin Liang); writing—original draft preparation, M.M.; writing—review and editing, M.M. and W.D.; visualization, W.D. and J.L. (Jianping Li); supervision, Z.W. and J.L. (Jin Liang); project administration, Z.W.; funding acquisition, Z.W. and M.M. All authors have read and agreed to the published version of the manuscript.

Funding: This work was funded by the National Key Research and Development Program of China (2024YFC2814700), the Guangdong Province Natural Science Foundation (2026A1515011054), the Post-subsidy Project of Guangzhou Marine Geological Survey, China (2025GMGS-HBZ-010 and 2025GMGS-HBZ-001), and the Hainan Province Key Research and Development Project (ZDYF2024GXJS002).

Data Availability Statement: Data will be made available on request. Further inquiries can be directed to the corresponding authors.

Acknowledgments: We thank the entire crew of Haiyangdizhi 4 for their support during data collection. We also sincerely appreciate the constructive comments from four anonymous reviewers, which have greatly improved the quality of the manuscript.

Conflicts of Interest: The authors declare no conflicts of interest.

Abbreviations

The following abbreviations are used in this manuscript:

MCSEM	marine controlled-source electromagnetic
BSR	Bottom Simulating Reflector
RMS	Root Mean Square
AVO	Amplitude Versus Offset

IHS	Intensity–Hue–Saturation
CDP	Common Depth Point
SEGY	Formats for seismic data

References

1. Collett, T.S. Energy resource potential of natural gas hydrates. *AAPG Bull.* **2002**, *86*, 1971–1992. [CrossRef]
2. Maslin, M.; Owen, M.; Day, S.; Long, D. Linking continental slope failures and climate change: Testing the clathrate gunhypothesis. *Geology* **2004**, *32*, 53–56. [CrossRef]
3. Sultan, N.; Cochonat, P.; Foucher, J.P.; Mienert, J. Effect of gas hydrates melting on seafloor slope instability. *Mar. Geol.* **2004**, *213*, 379–401. [CrossRef]
4. Klauda, B.; Sandler, S.l. Global distribution of methane hydrate in ocean sediment. *Energy Fuels* **2005**, *19*, 459–470. [CrossRef]
5. He, Z.X.; Yu, G. Marine Electromagnetic Exploration Technology and New Developments. *Prog. Explor. Geophys.* **2008**, *31*, 2–10. (In Chinese with English abstract)
6. Constable, S. Ten years of marine CSEM for hydrocarbon exploration. *Geophysics* **2010**, *75*, 75A67–75A81. [CrossRef]
7. Pei, F.; Fang, H.; Pei, L.; He, X.; Qiu, G. Advances in electromagnetic exploration research of gas hydrate. *Prog. Geophys.* **2020**, *35*, 775–785. (In Chinese with English abstract)
8. Schwalenberg, K.; Jegen, M. *Electromagnetic Applications in Methane Hydrate Reservoirs World Atlas of Submarine Gas Hydrates in Continental Margins*; Springer: Berlin/Heidelberg, Germany, 2022; pp. 73–85.
9. Goto, T.N.; Kasaya, T.; Takagi, R.; Sakurai, N.; Harada, M.; Sayanagi, K.; Kinoshita, M. Methane Hydrate Detection with Marine Studies off Japan Coast. In *Electromagnetic Surveys; Case OCEANS 2009-Europe*; IEEE: Piscataway, NJ, USA, 2009.
10. Hsu, S.; Chiang, C.; Evans, R.L.; Chen, C.; Chiu, S.; Ma, Y.; Chen, S.; Tsai, C.; Lin, S.; Wang, Y. Marine controlled source electromagnetic method used for the gas hydrates investigation in the offshore area of SW Taiwan. *J. Asian Earth Sci.* **2014**, *92*, 224–232. [CrossRef]
11. Weitemeyer, K.A.; Constable, S.; Shelander, D.; Haines, S. Mapping the resistivity structure of Walker Ridge 313 in the Gulf of Mexico using the marine CSEM method. *Mar. Pet. Geol.* **2017**, *88*, 1013–1031. [CrossRef]
12. Attias, E.; Weitemeyer, K.; Holz, S.; Naif, S.; Minshull, T.A.; Best, A.I.; Haroon, A.; Jegen-Kulcsar, M.; Berndt, C. High resolution resistivity imaging of marine gas hydrate structures by combined inversion of CSEM towed and ocean-bottom receiver data. *Geophys. J. Int.* **2018**, *214*, 1701–1714. [CrossRef]
13. Jing, J.; Chen, K.; Deng, M.; Zhao, Q.; Luo, X.; Tu, G.; Wang, M. A marine controlled-source electromagnetic survey to detect gas hydrates in the Qiongdongnan Basin, South China Sea. *J. Asian Earth Sci.* **2019**, *171*, 201–212. [CrossRef]
14. Jing, J.; Zhao, Q.; Deng, M.; Luo, X.; Chen, K.; Wang, M.; Tu, G. A study on natural gas hydrates and their forming model using marine controlled source electromagnetic survey in the Qiongdongnan basin. *Chin. J. Geophys.* **2018**, *61*, 4677–4689. (In Chinese with English abstract)
15. Jing, J.; Zhao, Q.; Luo, X.; Liu, C.; Chen, K.; Wang, M.; Deng, M.; Wu, Z. Marine controlled source electromagnetic imaging of gas hvdrates and gas sources in the Shenhu area, South China Sea. *Acta Geol. Sin.* **2024**, *98*, 2694–2708. (In Chinese with English abstract)
16. Haber, E.; Gazit, M.H. Model fusion and joint inversion. *Surv. Geophys.* **2013**, *34*, 675–695. [CrossRef]
17. Lyrio, J.C.S.O.; Menezes, P.T.L.; Correa, J.L.; Viana, A.R. Multiphysics anomaly map: A new data fusion workflow for geophysical interpretation. *Interpretation* **2020**, *8*, B35–B43. [CrossRef]
18. Cooper, G.R.J.; Cowan, D.R. Edge enhancement of potential-field data using normalized statistics. *Geophysics* **2008**, *73*, H1–H4. [CrossRef]
19. Erkan, K.; Christopher, J.; Shum, C.K. Fusion of gravity gradient and magnetic field data for discrimination of anomalies using deformation analysis. *Geophysics* **2012**, *77*, F13–F20. [CrossRef]
20. Altundas, Y.B.; Chugunov, N. Multiphysics fluid monitoring: Toward targeted monitoring design under uncertainty. *Interpretation* **2018**, *6*, SG19–SG32. [CrossRef]
21. Liu, J.; Zhang, J. New development of gravity-seismic joint inversion framework and application. *Prog. Geophys.* **2020**, *35*, 743–752. (In Chinese with English abstract)
22. Li, C.; Gong, W.; Zhao, L.; Li, Z.; Zhi, P.; Ge, J. Gravity-Seismic Joint Inversion of Lithospheric Density Structure in the Qiongdongnan Basin, Northwest South China Sea. *Lithosphere* **2024**, *2024*, 1–13. [CrossRef]
23. Li, J.; Ye, J.; Qin, X.W.; Qiu, H.J.; Wu, N.Y.; Lu, H.L.; Xie, W.W.; Lu, J.A.; Peng, F.; Xu, Z.Q.; et al. The first offshore natural gas hydrate production test in South China Sea China. *Geology* **2018**, *1*, 5–16. [CrossRef]

24. Li, S.; Chu, F.; Fang, Y.; Wu, Z.; Ni, Y. Associated interpretation of sub-bottom and single-channel seismic profiles from slope of Shenhu Area in the northern South China Sea-characteristics of gas hydrate sediment. *J. Trop. Oceanogr.* **2010**, *29*, 56–62. (In Chinese with English abstract)
25. Zhang, W.; Liang, J.; Wei, J.; Su, P.; Lin, L.; Huang, W. Origin of natural gases and associated gas hydrates in the Shenhu area, northern South China Sea: Results from the China Gas Hydrate Drilling Expeditions. *J. Asian Earth Sci.* **2019**, *183*, 103953. [CrossRef]
26. Liang, J.; Wang, H.; Su, X.; Fu, S.Y.; Wang, L.F.; Guo, Y.Q.; Chen, F.; Shang, J.J. Natural gas hydrate formation conditions and the associated controlling factors in the northern slope of the South China Sea. *Nat. Gas Ind.* **2014**, *34*, 128–135. (In Chinese with English abstract)
27. Zhong, Z.; Shi, H.; Zhu, M.; Xiong, P.; Min, H.; Zhao, Z.; Liu, S.; Fei, W. A discussion on the tectonic-stratigraphic framework and its origin mechanism in Pearl River Mouth Basin. *China Offshore Oil Gas* **2014**, *26*, 20–29. (In Chinese with English abstract)
28. Shi, H.; He, M.; Zhang, L.; Yu, Q.; Pang, X.; Zhong, Z.; Liu, L. Hydrocarbon geology, accumulation pattern and the next exploration strategy in the eastern Pearl River Mouth basin. *China Offshore Oil Gas* **2014**, *26*, 11–22. (In Chinese with English abstract)
29. He, M.; Zhong, G.; Liu, X.; Liu, L.; Shen, X.; Wu, Z. Rapid post-rift tectonic subsidence events in the Pearl River Mouth Basin, northern South China Sea margin. *J. Asian Earth Sci.* **2017**, *147*, 271–283. [CrossRef]
30. Lei, C.; Ren, J.; Pei, J.; Liu, B.; Zuo, X.; Liu, J. Tectonics of the offshore Red River Fault recorded in the junction of the Yinggehai and Qiongdongnan Basins. *Sci. China Earth Sci.* **2021**, *64*, 1893–1908. [CrossRef]
31. He, J.; Yan, W.; Zhu, Y.; Zhang, W.; Gong, F.; Liu, S.; Zhang, J.; Gong, X. Bio genetic and sub-biogenetic gas resource potential and genetic types of natural gas hydrates in the northern marginal basins of South China Sea. *Nat. Gas Ind.* **2021**, *33*, 121–134. (In Chinese with English abstract)
32. Lai, H.; Qiu, H.; Kuang, Z.; Ren, J.; Fang, Y.; Liang, J.; Lu, J.; Su, X.; Guo, R.; Yang, C.; et al. Integrated signatures of secondary microbial gas within gas hydrate reservoirs: A case study in the Shenhu area, northern south China sea. *Mar. Pet. Geol.* **2022**, *136*, 105486. [CrossRef]
33. Shi, W.; Song, Z.; Wang, X.; Kong, L. Diapir structure and its origin in the Baiyun Depression, Pearl River Mouth Basin, China. *Earth Sci.-J. China Univ. Geosci.* **2009**, *34*, 778–784. (In Chinese with English abstract)
34. Su, M.; Tiago, M.A.; Li, W.; Sha, Z.; Hsiung, F.; Liang, J.; Kuang, Z.; Wu, N.; Zhang, B.; Chiang, C. Reassessing two contrasting Late Miocene-Holocene stratigraphic frameworks for the Pearl River Mouth Basin, northern South China Sea. *Mar. Pet. Geol.* **2019**, *102*, 899–913. [CrossRef]
35. Wang, X.; Zhou, J.; Li, L.; Jin, J.; Li, J.; Guo, Y.; Wang, B.; Sun, L.; Qian, J. Bottom Simulating Reflections in the South China Sea. In *World Atlas of Submarine Gas Hydrates in Continental Margins*; Springer: Berlin/Heidelberg, Germany, 2022; pp. 163–172.
36. Li, J.P.; Chen, X.; Meng, D.J.; Yu, P.; Jing, J.E.; Luo, X.H.; Liu, Y.H.; Wang, M.; Chen, K.; Su, P.B.; et al. Combined interpretation of marine CSEM and reflection seismic data for gas hydrate characterization in the Shenhu area, South China Sea. *Chin. J. Geophys.* **2026**, *69*, 1412–1426. (In Chinese with English abstract)
37. Al-Chalabi, M. Time-depth relationships for multilayer depth conversion. *Geophys. Prospect.* **1997**, *45*, 715–720. [CrossRef]
38. Prez, P.; Gangnet, M.; Blake, A. Poisson image editing. *ACM Trans. Graph.* **2003**, *22*, 313–318. [CrossRef]
39. Agarwala, A.; Dontcheva, M.; Agrawala, M.; Drucker, S.; Colburn, A.; Curless, B.; Salesin, D.; Cohen, M. Interactive digital photomontage. *ACM Trans. Graph.* **2004**, *23*, 294–302. [CrossRef]
40. Liang, J.; Sha, Z.; Meng, M.; Wang, X.; Xu, M.; Fang, Y. Characteristics and distribution of gas hydrate bearing sediments with high saturation in the Shenhu area, South China Sea. *Acta Geol. Sin.* **2024**, *98*, 2641–2653. (In Chinese with English abstract)
41. Liang, J.; Meng, M.; Liang, J.; Ren, J.; He, Y.; Li, T.; Xu, M.; Wang, X. Drilling Cores and Geophysical Characteristics of Gas Hydrate-Bearing Sediments in the Production Test Region in the Shenhu sea, South China sea. *Front. Earth Sci.* **2022**, *10*, 1–14. [CrossRef]
42. Zhang, W.; Liang, J.; Su, P.; Wei, J.; Sha, Z.; Lin, L.; Liang, J.; Huang, W. Migrating pathways of hydrocarbons and their controlling effects associated with high saturation gas hydrate in Shenhu area, northern South China Sea. *Geol. China* **2018**, *45*, 1–14. (In Chinese with English abstract)
43. Sun, L.; Wang, X.; He, M.; Jin, J.; Li, J.; Li, Y.; Zhu, Z.; Zhang, G. Thermogenic gas controls high saturation gas hydrate distribution in the Pearl River Mouth Basin: Evidence from numerical modeling and seismic anomalies. *Ore Geol. Rev.* **2020**, *127*, 103846. [CrossRef]
44. Wu, N.; Yang, S.; Wang, H.; Liang, J.; Gong, Y.; Lu, Z.; Wu, D.; Guan, H. Gas-bearing fluid influx sub-system for gas hydrate geological system in Shenhu Area, Northern South China Sea. *Chin. J. Geophys.* **2009**, *52*, 1641–1650. (In Chinese with English abstract)

45. Qiao, S.; Su, M.; Yang, R.; Su, P.; Kuang, Z.; Sha, Z.; Liang, J.; Lu, H.; Xu, W.; Wu, N. Migration and Accumulation System: The Key Control Factors of Heterogeneous Distribution of Gas Hydrate. *Adv. New Renew. Energy* **2013**, *1*, 245–256. (In Chinese with English abstract)
46. Ren, J.; Cheng, C.; Jiang, T.; Kuang, Z.; Lai, H.; Liang, J.; Chen, Z.; Li, T. Faults and gas chimneys jointly dominate the gas hydrate accumulation in the Shenhu Area, northern South China Sea. *Front. Mar. Sci.* **2023**, *10*, 1254410. [CrossRef]